Received 31 December 2021; revised 12 February 2022; accepted 1 March 2022. Date of publication 10 March 2022; date of current version 22 March 2022.

Dividal Object Identifier 10.1109/OJCOMS.2022.3158310

Design and Evaluation of Reconfigurable Intelligent Surfaces in Real-World Environment

GEORGIOS C. TRICHOPOULOS¹⁰, PANAGIOTIS THEOFANOPOULOS, BHARATH KASHYAP, ADITYA SHEKHAWAT, ANUJ MODI¹⁰, TAWFIK OSMAN, SANJAY KUMAR, ANAND SENGAR, ARKAJYOTI CHANG, AND AHMED ALKHATEEB¹⁰

School of Electrical, Computer and Energy Engineering, Arizona State University, Tempe, AZ 85281, USA CORRESPONDING AUTHOR: A. ALKHATEEB (e-mail: aalkhateeb@asu.edu)

ABSTRACT Reconfigurable intelligent surfaces (RISs) have promising coverage and data-rate gains for wireless communication systems in 5G and beyond. Prior work has mainly focused on analyzing the performance of these surfaces using simulations or lab-level prototypes. To draw accurate insights about the actual performance of these systems, this paper develops an RIS proof-of-concept prototype and extensively evaluates its potential gains in the field under realistic wireless communication settings. In particular, a 160-element RIS, operating at a 5.8 GHz band, is designed, fabricated, and accurately measured in the anechoic chamber. This surface is then integrated into a wireless communication system and the beamforming gains, pathloss, and coverage improvements are evaluated in realistic outdoor communication scenarios. When both the transmitter and receiver employ directional antennas, the developed RIS achieves 15-20 dB gain in the signal-to-noise ratio (SNR) in a range of $\pm 60^{\circ}$ beamforming angles. In terms of coverage, and considering a far-field experiment with a blockage between a basestation and a grid of mobile users and with an average signal path of 35 m, the RIS provides an average SNR improvement of 6 dB (max 8 dB) within an area > 75 m². Thanks to the scalable RIS design, these SNR gains can be directly increased with larger RIS areas. For example, a single 1,600-element RIS with the same design is expected to provide 26 dB SNR gain for a similar deployment (theoretical estimation). These results draw useful insights into the design and performance of RIS systems and provide an important proof for their potential gains in real-world far-field wireless communication environments.

INDEX TERMS Reconfigurable intelligent surfaces, prototype, beamforming, coverage, sub-6GHz.

I. INTRODUCTION

RECONFIGURABLE Intelligent Surfaces (RISs) have attracted significant interest in the recent years from both academia and industry [1]–[4]. This is motivated by the promising gains that RISs are envisioned to offer for both millimeter wave (mmWave)/terahertz (THz) and sub-6GHz wireless communication systems. At mmWave/THz bands, RIS surfaces provide a potential solution for the critical coverage challenge by intelligently reflecting/refracting the wireless signals to the receiver direction [5]–[11]. At sub-6 GHz bands, RIS systems could be leveraged to enhance the propagation characteristics [12], [13] and increase the spatial multiplexing gains. RISs also find interesting applications in localization [14], sensing [15],

and in enhancing the security of the wireless communication systems [16], [17]. For example, RISs can suppress signals propagating toward eavesdroppers by creating "quite" zones around suspicious user equipment (UE). Thus, RISs can modify the channel appropriately and provide physical layer security in wireless networks [18]–[20]. With all this potential, it is important to accurately evaluate the performance of the RIS surfaces in reality. Based on this motivation, this work considers designing a low-power and portable proof of concept prototype for RIS-integrated wireless communications systems and leveraging it to validate the potential RIS gains in realistic communication environments. Next, we provide a brief background for the RIS circuits and systems before reviewing the relevant prior work

This work is licensed under a Creative Commons Attribution-NonCommercial-NoDerivatives 4.0 License. For more information, see https://creativecommons.org/licenses/by-nc-nd/4.0/

in Section I-B and summarizing the key contributions in Section I-C.

A. A BRIEF BACKGROUND

RISs comprise reconfigurable reflective surfaces that employ tunable subwavelength structures (e.g., microstrip patches) to modulate the phase and/or amplitude of reflected waves. A smooth flat surface (e.g., mirror) reflects signals in the specular direction (incident angle = angle of reflection) because of the predetermined constant phase delay induced as the wave traverses the surface. On the other hand, RISs are capable of anomalous reflection (angle of reflection ≠ incident angle) by artificially modulating the phase and/or amplitude of the reflected wave [21]. Besides redirecting the signal to desired directions in the far-field, RISs can also focus the energy when the UE or the base station (BS) is in the radiating near-field of the RIS. The sub-wavelength unit cell receives the incident signal and re-radiates it back into free space with a different amplitude and/or phase. Such modulation can be achieved by tuning the electromagnetic properties of the unit cell. For example, a switch placed at the feed of a resonant metallic patch can alter the path of the electric current (open/short termination) and modulate the amplitude and phase of the re-radiated field. More switches can allow multi-bit wavefront modulation with improved beam control and efficiency. Several topologies can be found in the literature using single or multiple active devices as well as single or multi-layered substrates [22]. In all approaches, a biasing circuit and control unit (e.g., microcontroller) is required to be integrated within the RIS to control the state of the tunable devices by varying the biasing voltage across the device terminals. RISs are considered two-dimensional structures because the lateral dimensions are multiple wavelengths and thickness only a fraction of a wavelength. Such geometrical properties could allow for seamless installation on building surfaces (indoors or outdoors) even on curved surfaces.

In mmWave and THz non-line-of-sight (NLoS) paths, if the user is not in the specular reflection direction, then communication relies on diffuse scattering [23] from the rough surfaces of the surroundings (e.g., walls, terrain). Unless the user is near the specular direction, signal strength is impacted drastically and enabling anomalous reflection can provide viable propagation paths and boost the strength of received signal. Using the bistatic radar equation, we can estimate the received power P_r when an RIS is placed between the UE and the BS, as illustrated in Fig. 1:

$$P_r = \frac{P_t G_{BS} G_{UE} \lambda^2 \sigma}{(4\pi)^3 R_i^2 R_d^2} \tag{1}$$

where P_t is the signal power transmitted by the BS, G_{BS} , G_{UE} are the gains of the BS and UE antennas respectively, R_i and R_d the distances between BS-RIS and RIS-UE. The radar cross section σ of the RIS can be approximated as a rectangular, flat conductive surface with losses. As such, the

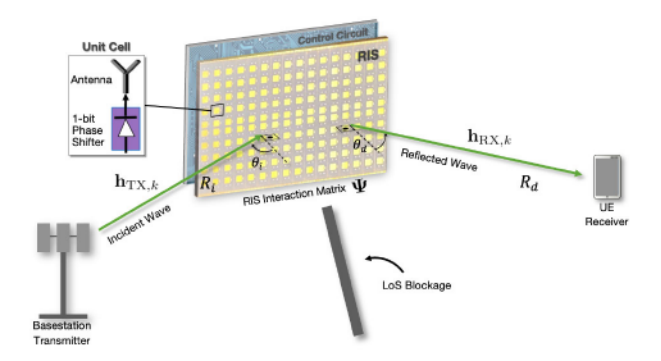


FIGURE 1. Overview of the proposed reconfigurable intelligent surface (RIS). A control circuit provides the necessary excitation (beamforming weights) to the unit cells and redirects the incident wave to the desired direction.

monostatic RCS of the an electrically large RIS with area A, efficiency η , and wavelength λ is:

$$\sigma = \frac{4\pi \eta A^2}{\lambda^2} \tag{2}$$

In a bistatic scenario, similar to the deployments in wireless communications, the RIS is viewed with an angle θ_i from the BS and θ_d from the UE (as shown in Fig. 1), assuming BS and UE are on the same plane. Then, the bistatic RCS of the RIS can be approximated by:

$$\sigma = \frac{4\pi \eta cos\theta_i cos\theta_d A^2}{\lambda^2} \tag{3}$$

We notice here that the received power increases quadratically with the size of the RIS. Namely, a ten-fold increase in the area A provides 20 dB stronger signal for the same propagation scenario. Similarly, using RISs in higher frequencies, the received power will increase inversely proportional to the square of the wavelength. Such signal improvement is also crucial when considering that higher frequency signals suffer more losses (e.g., free path loss, penetration loss). For example, a window glass or a brick wall can have attenuation that exceeds 25 dB and 91 dB respectively at 38 GHz [24].

B. PRIOR WORK ON RECONFIGURABLE INTELLIGENT SURFACES

The design and analysis of RIS-integrated wireless communication systems have attracted significant interest in the last few years. From the signal processing perspective, RIS systems bring interesting challenges to the design of the large-dimensional passive beamforming matrices at the RIS surfaces. For example, [25] investigates the design of low-complexity and energy-efficient RIS beamforming algorithms, [26] designs robust RIS beamforming solutions, and [27]–[29] develop techniques for the joint basestation-RIS beamforming design problem. One main critical challenge for the operation of these systems is the high training overhead associated with the channel acquisition, especially if these surfaces are nearly passive. To address this challenge, [4] developed RIS architectures where sparse active elements can be leveraged to acquire some knowledge about

the channel. This can also enable leveraging compressive sensing and deep learning approaches to efficiently estimate the RIS channels [4]. From the network perspective, prior work has analyzed the covcerage performance in outdoor or indoor settings utilizing the RIS for reflection [5]–[8], refraction to enhance the outdoor-to-indoor coverage [9], and for joint transmission and reflection [10], [11]. The prior work in [4]–[9], [25]–[29], however, was mainly limited to simulation data. To accurately evaluate the potential of the RIS surfaces, it is crucial to build proof-of-concept prototypes and assess the expected coverage and data rate gains of RIS-integrated systems in real world wireless communication environments.

From the circuits and prototyping perspectives, various tuning topologies have been reported in the microwave frequency region using PIN or varactor diodes [30]-[32]. These topologies are used as beamformers in wireless communications, imaging, and sensing. In [33], an implementation of a reconfigurable intelligent surface was presented where the authors showed an indoor coverage analysis using a 2.4 GHz 3,200-element RIS. The user and/or base station, however, were in the near field of surface. In [34], the authors presented a sub-6 GHz metasurface-based RIS to enhance received signal in wireless communication systems. Although the work shows clear improvement in the received signal, the experiments are limited to topologies where (i) both the receiver and transmitter are coupled to directive antennas and (ii) the receiver is always in the near field of the RIS. Additionally, the RIS prototype uses varactor switches, unit cells smaller than $\lambda/2$, vias, and a multilayered PCB structure, which is a viable solution for microwave frequencies, but a non-scalable approach for mmWave and THz frequencies. This highlights the need to develop more efficient prototyping approaches for RIS systems and accurately evaluate their performance in realistic wireless communication scenarios where both the transmitter and receiver are in the far-field of the RIS surface.

Reconfigurable surfaces (either mirror or lenses) have also been implemented in the mmWave bands using also PIN diodes [35] and there are many research efforts for higher frequency topologies approaching the THz bands [36]. However, new switching topologies and materials are required (e.g., VO2, graphene, liquid crystal) to overcome the limited performance of PIN and varactor diodes [37] and simplified unit cell layouts to enable practically manufacturability of mmWave and THz RISs [38]-[41]. For the RIS to be attractive in wireless communications, the surface needs to be scalable to large areas with thousands of unit cells and switches, low-profile and conformal to fit in various irregular indoor or outdoor surfaces, consume low power, and be cost efficient in manufacturing, installation, and maintenance. Although most of these features are inherent in reflective surfaces, switching performance and manufacturability due to the biasing circuit topologies are engineering challenges.

C. CONTRIBUTION

In this paper, we designed and fabricated a low-power reconfigurable intelligent surface and demonstrated its beamforming and coverage gain potential capabilities in real-world wireless communications environments. The main contributions can be summarized as follows:

- Present a single layer, single switch-per-cell RIS design operating at 5.8 GHz that is also compatible with mmWave and THz fabrication and integration technologies. The layout requires no vertical connections (e.g., vias) and biasing network in integrated on the same plane. The RIS is capable of electronic beam scanning in both azimuth and elevation planes.
- Characterize the beamforming capabilities in an outdoor environment. We carried out radiation pattern characterization in the controlled environment of an anechoic chamber and then evaluated the beamforming gains in realistic near-field and far-field outdoor settings in the presence of scattering from the ground and the surrounding environment.
- Carry out coverage measurements at 5.8 GHz in occluded (line-of-sight (LoS) obstructed), outdoor areas using mobile UE with omni-directional antennas. The LoS path between the BS and mobile UE is blocked by a building and the signal coverage is improved when using the proposed RIS to provide an alternative signal path.

The paper is structured as follows: In Section II, we present current RIS design and discuss the fundamental operation of reflectarray antennas, which is a main component in RISs. In Section III, we discuss the quantized beamforming theory of RISs and its relationship to wireless communication between a BS and UE. Then, Section IV presents the design and characterization of the RIS, including a discussion on the unit cell layout (building block of the RIS), testing of the integrated switches and beamforming, and integration with the necessary control circuitry. In Section V, we present a wireless communication testbed - including a BS, UE, and the RIS - to evaluate the performance of the RIS in realsitic wireless communication field tests. Finally, in Section V, we evaluate the potential gains of the RIS beamforming in improving the SNR at the mobile users and extending the wireless communication coverage beyond LoS areas.

II. RIS-BASED WIRELESS COMMUNICATION SYSTEM

In this section, we describe the adopted RIS-assisted wireless communication system and briefly formulate the beamforming design problem.

A. SYSTEM AND SIGNAL MODELS

As depicted in Fig. 1, we consider a simple scenario where the communication between a single-antenna transmitter and a single-antenna receiver is assisted by a reconfigurable intelligent surface. The surface is assumed to have a uniform planar array structure of $M \times N$ elements. Adopting an OFDM

(Orthogonal Frequency Division Multiplexed) system model with K sub-carriers, we define $\mathbf{h}_{\mathrm{TX},k}$ and $\mathbf{h}_{\mathrm{RX},k}$ as the kth subcarrier $MN \times 1$ uplink channels from the transmitter and receiver to the RIS, $k = 1, 2, \ldots, K$. Further, we define $h_{\mathrm{TR},k}$ as the direct LoS channel between the transmitter and receiver on the kth subcarrier. If s_k denotes the transmitted signal over the kth subcarrier, then the received signal can be written as

$$r_k = \mathbf{h}_{\mathrm{RX},k}^T \Psi \mathbf{h}_{\mathrm{TX},k} s_k + h_{\mathrm{TR},k} s_k + n_k, \tag{4}$$

where $n_k \sim \mathcal{N}_{\mathbb{C}}(0, \sigma_n^2)$ represents the receive noise and s_k has an average power $\mathbb{E}[s_k] = \frac{P}{K}$ with P representing the total transit power. The matrix Ψ denotes the $MN \times MN$ RIS interaction matrix. Note that Ψ is a diagonal matrix. To capture that, we define $\psi = \operatorname{diag}(\Psi)$ as the $MN \times 1$ RIS reflection vector, which includes the phase control at each RIS element. In particular, each element mn is expressed as $e^{j\varphi_{mn}}$, with the φ_{mn} denoting the RIS modulation phase of this element. Now, neglecting the LoS link (for the scenarios with blocked LoS), the RIS beamforming/excitation vector ψ can be designed to maximize the achievable rate following

$$\psi^{\star} = \arg \max_{\varphi_{mn}, \forall m, n} \sum_{k=1}^{K} \log_2 \left(1 + \rho \left| \mathbf{h}_{\mathrm{RX}, k}^H \mathbf{\Psi} \mathbf{h}_{\mathrm{TX}, k} \right|^2 \right), \quad (5)$$
s.t.
$$\varphi_{mn} \in \left[0^{\circ}, 360^{\circ} \right], \quad \forall m, n, \quad (6)$$

where $\rho = \frac{P}{K\sigma_n^2}$ denoting the per-carrier SNR. Next, since the RIS-transmitter and RIS-receiver channels are mostly dominated by LoS paths, we consider the following approaximation for the design of the RIS reflection vector

$$\psi^{\star} = \arg \max_{\varphi_{mn}, \forall m, n} \sum_{k=1}^{K} \left| \mathbf{h}_{\mathrm{RX}, k}^{H} \Psi \mathbf{h}_{\mathrm{TX}, k} \right|^{2}, \tag{7}$$

s.t.
$$\varphi_{mn} \in [0^{\circ}, 360^{\circ}], \forall m, n.$$
 (8)

In practice, the channels between the RIS and the transmitters/receivers will likely be LoS. Now, focusing on this case, the optimization problem in (7)-(8) can be further reduced to

$$\psi^{\star} = \arg \max_{\varphi_{mn}, \forall m, n} \left| \left(\mathbf{a}_{RIS}^{*}(\theta_{d}, \phi_{d}) \odot \mathbf{a}_{RIS}(\theta_{i}, \phi_{i}) \right)^{T} \psi \right|^{2}, (9)$$
s.t. $\varphi_{mn} \in [0^{\circ}, 360^{\circ}], \forall m, n.$ (10)

where $a_{RIS}(\theta,\phi)$ denotes the RIS array response vector for the angles θ,ϕ . The angles θ_i and ϕ_i represent the elevation/azimuth angles of the incident signal and the angles θ_d and ϕ_d represent the elevation/azimuth angles of the desired reflection direction. In the next subsection, we briefly present the design approach for the beamforming codebook adopted in this work.

B. 1-BIT BEAMFORMING CODEBOOK

Consider the RIS beamforming design problem in (9)-(10), if the incident and desired reflection directions are (θ_i, ϕ_i) and (θ_d, ϕ_d) , respectively, then the optimal RIS phase shifting configuration for each element φ_{mn} in ψ is given by

$$\varphi_{mn} = \varphi_{i,mn} - \varphi_{d,mn}, \tag{11}$$

where $\varphi_{i,mn}$ and $\varphi_{d,mn}$ are respectively the phase of the incident wave and phase for the desired reflection direction on the mn^{th} RIS unit cell. For a two-dimensional planar RIS with unit cells arranged on the x-y plane, these phases are given by [42]

$$\varphi_{i,mn} = k_0(x_m \sin \theta_i \cos \phi_i + y_n \sin \theta_i \sin \phi_i), \qquad (12)$$

$$\varphi_{d,mn} = k_0(x_m \sin \theta_d \cos \phi_d + y_n \sin \theta_d \sin \phi_d), \quad (13)$$

with k_0 representing the free space wavenumber and (x_m, y_m) are the coordinates of the mnth RIS element. However, at mmWave/THz frequencies practical phase shifting topologies can only produce discrete values of φ_{mn} that are typically quantized using 1-, 2- or 3- bit quantization schemes. A single-bit phase quantization scheme is adopted in this work owing to its simplicity and lower cost when compared to higher bit quantization methods [43]. As such, all the phase values in the range $[-90^0, +90^0]$ are rounded off to 0^0 (designated as state '0'/OFF) and the rest of the phase values are rounded off to 1800 (designated as state '1'/ON). The two states are realized using PIN diodes with state '0' representing the OFF state of the diode and state '1' corresponding to the diode's ON state, as will be explained in detail in Section III. Thus, the quantized phase shift at the mnth RIS unit cell is:

$$\varphi_{mn}^{\text{quant}} = \left| 180^0 \cdot \text{round} \left(\frac{\varphi_{mn}}{180^0} \right) \right|.$$
 (14)

With this RIS beamforming design, the resulting far-field radiation pattern of the RIS at a direction θ , ϕ can be approximated by the array factor

$$AF_{RIS}(\theta, \phi) = \sum_{m=1}^{M} \sum_{n=1}^{N} e^{-jk_0(x_m u + y_n v)} e^{j\varphi_{i,mn}} e^{j\varphi_{mn}^{quant}}, \quad (15)$$

where $k_0(x_m u + y_n v)$ represents the phase modulation due to Green's function, with $u = \sin \theta \cos \phi$ and $v = \sin \theta \sin \phi$.

For efficient wireless communication operation with the RIS, we design a codebook \mathcal{P} of pre-defined beams (RIS phase shifting configuration). Each RIS beam codeword in this codebook reflects the wave that is incident from a direction (θ_i, ϕ_i) to a desired reflection direction (θ_d, ϕ_d) . For example, if the desired sets of directions for the incident and reflected waves are respectively defined by

$$\mathcal{I} = \left\{ (\theta_{i,1}, \phi_{i,1}), (\theta_{i,2}, \phi_{i,2}), \dots, (\theta_{i,N_i}, \phi_{i,N_i}) \right\}$$
(16)
$$\mathcal{D} = \left\{ (\theta_{i,1}, \phi_{i,1}), (\theta_{i,2}, \phi_{i,2}), \dots, (\theta_{i,N_i}, \phi_{i,N_i}) \right\}$$
(17)

$$\mathcal{D} = \left\{ \left(\theta_{d,1}, \phi_{d,1}\right), \left(\theta_{d,2}, \phi_{d,2}\right), \dots, \left(\theta_{d,N_d}, \phi_{d,N_d}\right) \right\}$$
(17)

with cardinalities $|\mathcal{I}| = N_i$ and $|\mathcal{D}| = N_d$, then the RIS codebook \mathcal{P} will have N_iN_d beam codewords. Each codeword vector $\overline{\psi}_{i,d} \in \mathcal{P}$ is designed following the 1-bit (quantized) beamforming approach in (11)-(14) for a particular incident/reflection directions from \mathcal{I} and \mathcal{D} . Additionally, the 1-bit quantization reduces the aperture efficiency η by

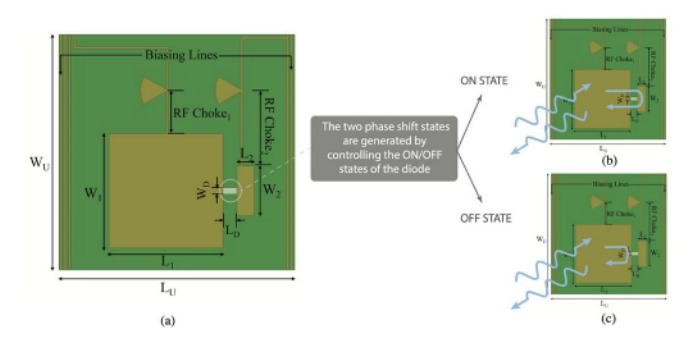


FIGURE 2. Layout of the RIS unit cell. (a) The unit cell consists of a main resonant metallic patch connected to a parasitic rectangular patch through an RF PIN diode (switch). The necessary biasing lines and RF chokes are integrated for switch activation (ON/OFF). (b), (c) Activation of the RF PIN diode alters the current distribution, resulting in phase modulation of the reflected signal (180 degrees) without a significant modulation of the magnitude within the bandwidth of interest.

TABLE 1. Key dimensions of the RIS unit cell.

Unit Cell Design Parameters	Dimension (mm)
W_{U}	25.85
W_1	12.51
L_1	12.51
W_2	5.48
$W_{\mathbf{D}}$	0.7
L_{D}	1.5

50% (see equation (1)) compared to an ideal continuously modulated phase.

III. RECONFIGURABLE INTELLIGENT SURFACE DESIGN

In this section, we present the design and characterization of the RIS, including the unit cell layout, measurement of the radiation pattern of both a fixed-beam (no switches) and a multi-beam RIS prototype (integrated PIN switches), and integration of the control circuitry. The RIS is designed at a center frequency of 5.8 GHz which is part of the unlicensed spectrum used in wireless local area networks (WLANs). The goal of this work is to design a single layer topology (besides the ground plane) without requiring the use of vertical components (e.g., vias). As such, the RIS is comprised of the ground plane, the substrate, and the top metalization layer. Such topology is attractive for future mmWave and THz RISs where multilayer structures increase losses and fabrication complexity.

A. 1-BIT UNIT CELL DESIGN

The RIS comprises $160 (16 \times 10)$ unit cells that contain a resonant metallic patch, a radio-frequency (RF) PIN diode (switch), and biasing lines, as shown in Fig. 2 and Fig. 3. Depending on the applied voltage across the diode terminals (reverse bias: OFF, forward bias: ON), the resonant patch re-radiates the received signal with a phase difference that depends on the current distribution. Typically, such a phase shift is enabled either by changing the resonant frequency of the patch [44], [45] or by providing extra path to the current on the feed of the patch [38], [46]. The latter approach

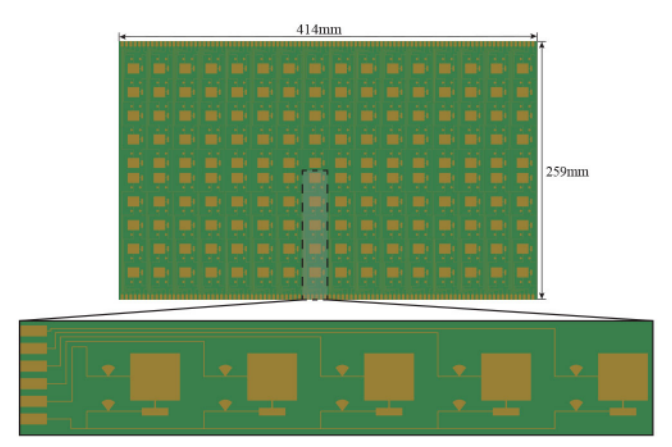
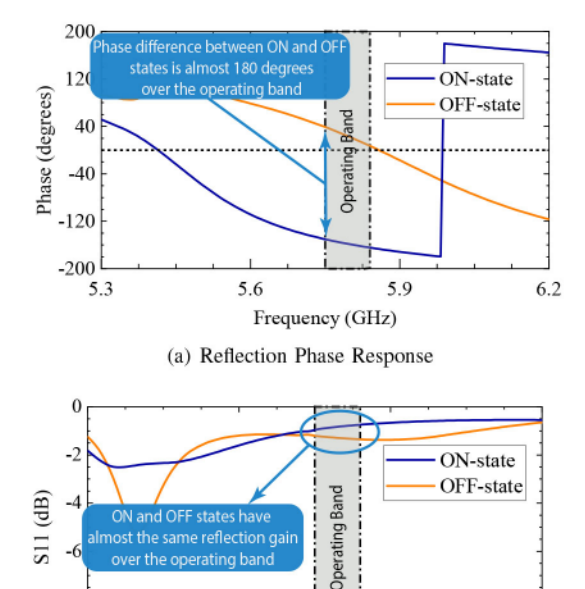


FIGURE 3. The layout of the 160-element (16 \times 10) array used in the proposed RIS. The inset shows the routing of the biasing lines for 5 unit cells (no vias). This constitutes a 2D topology that is compatible with low complexity RIS implementation in the mmWave and THz bands.

requires a short transmission line terminated to the ground. Such topology would require a via, thus, to minimize fabrication complexity, we opted for the resonance approach by adding a parasitic patch next to the main resonant patch connected through the PIN diode. Additionally, biasing lines are needed for both diode terminals, therefore, two narrow lines are connected to the main patch and the parasitic patch respectively, as depicted in Fig. 2.

To isolate the RF signal from the biasing lines, a radial stub is used in each one of the lines. The biasing lines are routed in groups of five unit cells to ensure minimum wiring complexity, as shown in the full array topology in Fig. 3. As opposed to current approaches in the literature, the proposed topology 1) requires only a single tuning device (switch) and 2) comprises a single layer with no vertical connections to the ground. Although single switch approaches result in quantization sidelobes, in this study, we use the RIS only in limited scanning range to avoid sidelobe interference. Nevertheless, using pre-coded, phase randomization methods [38], [47] we can eliminate the undesired side lobes using practical topologies. This step has not been the focus of this work and is left for future prototype implementations. Additionally, phase quantization can also limit the minimum step in beamscanning. For the 1-bit topology presented here, beamstep is limited to approximately one half-power beamwidth (HPBW). As such, for a 1-bit RIS with a HPBW of 6°, the beamscanning step is also 6° when scanning close to boresight. The step will increase when scanning at wider angles close to the horizon. Although further investigation is required, RIS phase quantization appears to have a limited effect on channel coverage [38], [48].

To evaluate the response of the unit cell under different biasing states, we use an industry standard commercial electromagnetics (EM) solver (ANSYS, HFSS). As such, we design an infinite array of unit cells using periodic boundary conditions on each primary direction [49]. Although this process omits radiation effects at the edge of the aperture, it is considered reliable in estimating the EM response of an



(b) Reflection Magnitude Response

Frequency (GHz)

6.2

FIGURE 4. Numerical analysis (periodic boundary conditions) of the unit cell response under boresight illumination ($\theta_I = 0$) for two switch states (ON/OFF).

5.6

individual unit cell. The substrate used here is Rogers RT/ Duroid 6002 RF laminate with dielectric constant, height and loss tangent of 2.94, 2.54 mm, 0.0012 respectively. The microstrip patch/switch (BAR50-02V) co-design is carried out using the measured S-parameters provided by the manufacturer (MACOM). In the infinite array model of the RIS, we compute the reflected signals on a Floquet port under boresight illumination ($\vartheta_i = 0$). As shown in Fig. 4, the difference in the magnitude of the reflected signal is kept small (< 1 dB) between the two states while the phase difference is 180° at 5.8 GHz. For an acceptable phase modulation range of $180^{\circ} \pm 20^{\circ}$ between the two states, the expected bandwidth is approximately 150 MHz, as shown in Fig. 4. We mention here, that the angle of incidence and the mutual coupling (finite array) will also affect the magnitude and phase response and will determine the overall scanning and bandwidth performance of the RIS. We further evaluate this in Section III-E. Next, we integrate the unit cells into a large array and analyze the radiation effects under various switch excitations (codebook).

B. ARRAY DESIGN

-8

5.3

The radiation characteristics of the RIS have been studied using both the analytical expression of Eq. (14) as well as using a full-wave numerical method. To account for the electrically large model, we used ANSYS HFSS finite element boundary integral (FE-BI) which reduces the computational complexity. In the first scenario, we model the RIS with a feed horn antenna ($\theta_i = -27.5^{\circ}$) and calculate the radiation patterns for the excitation of three different reflection

angles (0°, 17°, and 60°). The three excitations result in distinct main lobes at the desired directions, as shown in the analytical and full-wave simulation results of Fig. 5. The discrepancy between the side lobe levels in Fig. 5a is attributed to the diffraction and surface wave phenomena that are not accounted for in the array factor analysis. Because most of the power is directed in the main beam, a similar discrepancy is not noticed in Fig. 5c. Nevertheless, measurement alignment errors can also contribute to the pattern discrepancies and further analysis is needed to understand the cause. Additionally, to simulate the beamforming characteristics when the feed is in the far-field, as expected in several wireless communications scenarios, we replace the feed horn antenna by a plane wave excitation and plot the normalized radar cross section (RCS) pattern for three reflection angles (22.5°, 40°, and 60°). Due to the phase quantization error, the reflected beam present a second grading lobe at the opposite angle around the specular direction, as shown in Fig. 6. The quantization lobes can be mitigated by adding random phase delays at each unit cell [38], [47].

C. CHARACTERIZATION OF A FIXED BEAM RIS

To evaluate the accuracy of the array design simulations, we fabricated a fixed beam reflectarray and measured the radiation pattern at 5.8 GHz. The RIS comprises 160 unit cells (16 × 10) with an overall array dimension of 414 mm \times 259 mm. In place of the RF PIN diodes, we place short or open terminations and design the RIS to operate as a reflectarray antenna with a reflection angle at +60°. Then the layout was fabricated using a chemical etching process on a 2.54 mm thick Rogers RT/duroid 6002 substrate. First, the array layout is printed on a thermal sheet using an inkjet printer and then heat pressed on the substrate at 530 C° . Afterward, the substrate with the imprinted mask is immersed into sodium persulphate $(Na_2S_2O_8)$ to etch the copper and the mask is removed using acetone. To test the radiation pattern, a 12.5 dBi feed horn antenna is fixed above the reflectarray at an angle of -27.5° , as depicted in Fig. 7. The measurement took place in an anechoic chamber (ASU's Compact Antenna Test Range) to ensure for minimum reflections from any surroundings. As plotted in Fig. 8, the normalized gain is measured in the $[-90^{\circ}, +90^{\circ}]$ range (E-plane) and shows good agreement with the full-wave numerical analysis.

D. IMPLEMENTATION OF THE RIS

In this section, we detail the fabrication and assembly of the RIS prototype. To verify the computed performance of the RF PIN diodes, we fabricated a test board that included several BAR50 PIN diodes with the necessary biasing contact pads and RF chokes, as shown in Fig. 9(a). Here, the diodes are terminated to a rectangular patch that is similar to the RIS unit cell topology, thus emulating a mismatch that generates around 180° phase difference in the reflected signal between the PIN diode's biasing states. Using a vector network analyzer (VNA), we first shift the reference plane to the SMA connectors of the

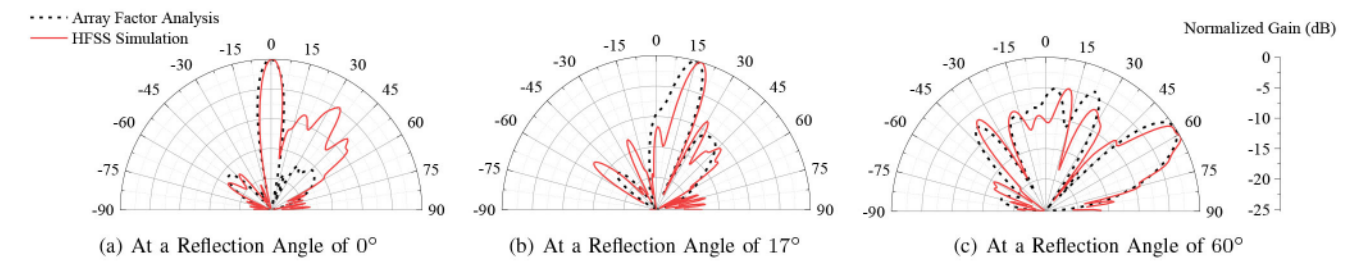


FIGURE 5. Computed radiation patterns when the RIS is illuminated by a feed horn antenna (near-field, $\theta_I = -27.5^{\circ}$) for various reflection angles (θ_d).

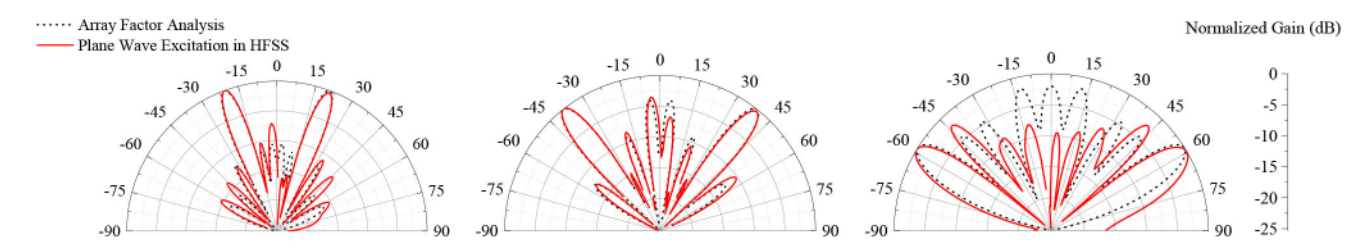


FIGURE 6. Computed RIS radar cross section patterns under plane wave illumination (normal incidence) for various reflections angles (\$\textit{t}_d\$): (a) 22.5°, (b) 40°, and (c) 60°.

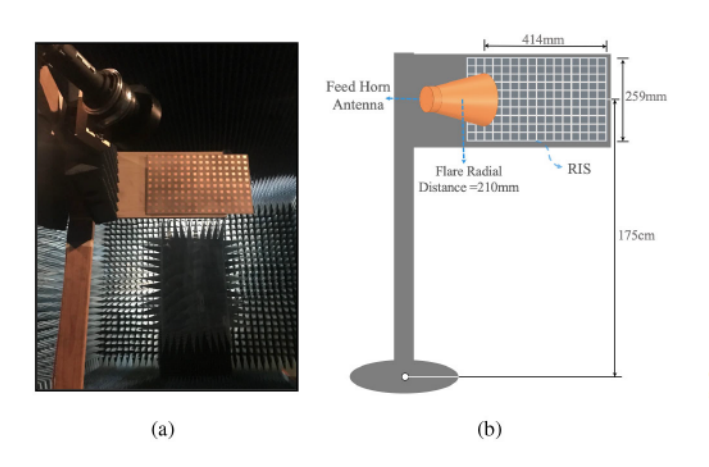


FIGURE 7. This figure illustrates the adopted measurement setup for the fixed-beam (passive) RIS prototype characterization. Figure (a) shows the anechoic chamber measurement setup and (b) summarizes the dimensions of the fixture.

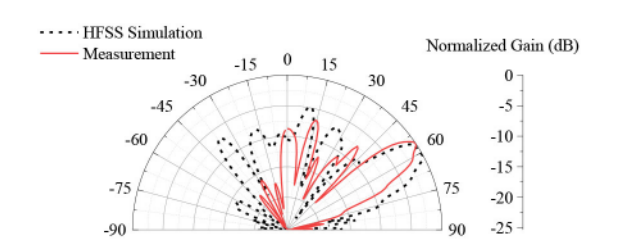


FIGURE 8. This figure shows a comparison between the measured (in the anechoic chamber) and computed radiation patterns of the 5.8 GHz fixed beam (passive) RIS prototype, which confirms the agreement between the designed and actual beams.

testboard using a one-port calibration and then deembed the measured reflection coefficient (S_{11}) of 4 test diodes for both biasing states by accounting for the length of the microstrip transmission line. As plotted in Fig. 9(b), the phase difference is around 171° for a wide frequency range around 5.8 GHz which is in accordance to the circuit simulations as well as the phase response of the unit cell around the design frequency (5.8 GHz),

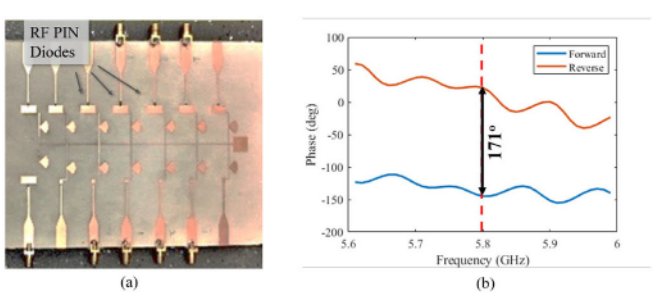


FIGURE 9. Testboard for the characterization of the RF PIN diode switch. (a) Layout of the testboard and (b) phase response of the reflected signal for two different switch states (forward/reverse blased).

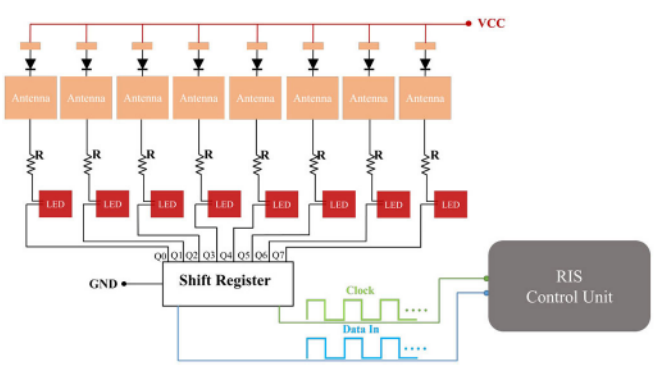


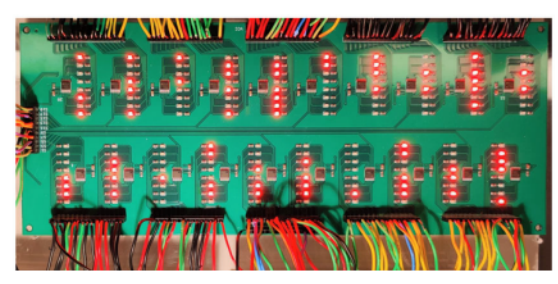
FIGURE 10. Schematic of the RIS control circuit. A codeword is generated and parsed to the RF PIN diodes through a microcontroller and 20 8-bit shift registers (LEDs are only needed for troubleshooting).

as presented in Fig. 4. Then, we assembled 160 diodes on the array and integrated them with the necessary control circuitry. Fig. 10 shows a schematic of the RIS control circuitry that comprises the biasing circuit and a micro-controller (which also stores the beam codebook).

The micro-controller (Arduino MEGA2560) splits the bit sequence of each codeword (which consists of 160 bits)



(a) RIS Front-End



(b) RIS Back-End

FIGURE 11. The developed 160-element RIS prototype at the sub-6 GHz band: Figure (a) shows the front-end which has the reflecting elements and figure (b) shows the back-end with the RIS control circuit.

into 10 segments, each corresponding to the configuration weights of 16 unit cells. Two clock signals, register clock (RCK) and shift register clock (SRCK), from the control unit are connected to all the shift registers in parallel for synchronization. The 8 bits on each shift register output pin are input serially and synchronized using the RCK. Finally, all the shift registers' outputs are activated in parallel using the SRCK. Every codeword segment is then pushed to a pair of in-series connected 8-bit shift registers (20 in total). As such, every output of a shift register is connected in series with an LED and resistor to provide 0.8 V across each PIN diode for forward biasing (0 V for reverse biasing) and limit the current to 3 mA. We note here that the LEDs are used only for debugging and testing purposes and are not necessary for the RIS operation. The minimum time required to update the excitation of all the RIS elements (switch ON/OFF status) is only limited by the clock maximum frequency of the biasing control circuit. Thus, the minimum delay is

$$t = \frac{n_{\rm p} N_{\rm s}}{f_{\rm mc}} = 1 \ \mu \text{sec} \tag{18}$$

where n_p is the number of bits of the shift registers ($n_p = 8$), N_s the number shift registers in series ($N_s = 2$), and f_{mc} the frequency of the microcontroller ($f_{mc,max} = 16$ MHz).

With this biasing circuit design, the bit sequence of each codeword determines the unit cell induced phased delay (0° or 180°) across the 160-element array, and thus steering the beam to the corresponding direction. Fig. 11 shows the front and rear side (control unit) of the RIS assembled on the

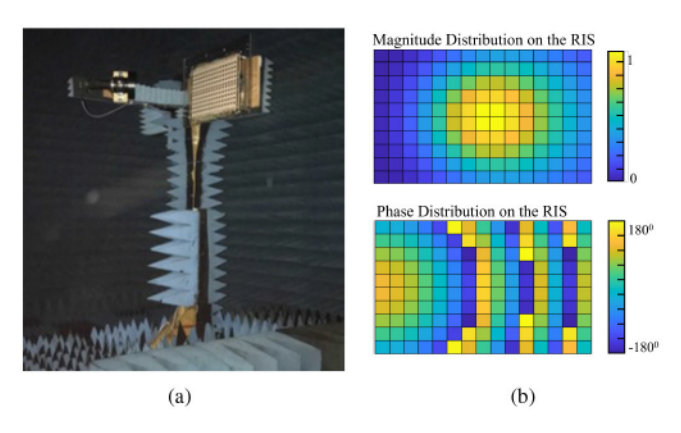


FIGURE 12. RIS characterization in the anechoic chamber. (a) Photo of the RIS setup in the chamber and (b) magnitude and phase distribution of the incident feed horn antenna beam on the RIS aperture.

fixture. Under typical RIS operation, approximately 50% of the diodes are ON, resulting in total power consumption of less than 0.4 W. The PIN diode and shift register consume 3 mW and 1.58 mW respectively, with a total consumption of 560 mW when all switches are ON. Additionally, the microcontroller consumes an average of 100 mW. We would like to mention here that various parameters determine the total DC power consumption of a deployed RIS, including the size of the aperture, the need for a wireless link to the network (signaling), and the type of the RF switches. For the later, power consumption can be dramatically reduced with transistor- based switches [50] to micro-Watt levels even for RISs with thousands of elements due to the small leakage current of such devices.

E. CHARACTERIZATION OF THE RIS BEAMFORMING

Similar to the fixed beam reflectarray measurement, the RIS is assembled with a feed horn antenna (near-field) inside the anechoic chamber, as shown in Fig. 12(a). Being in the nearfield, the feed horn impresses a Gaussian field distribution on the RIS aperture, as shown in the plots of magnitude and phase in Fig. 12(b). The recorded radiation patterns for 5 reflected directions ($\vartheta_d = \{0^\circ, 15^\circ, 30^\circ, 45^\circ, 60^\circ\}$) show very good agreement with the full-wave simulations, as plotted in Fig. 13. The right column in Fig. 13 shows the quantized phase distribution $\Phi^{quant} = (\phi_{mn}^{quant})$ when applying the respective codeword vectors $\overline{\psi}_{-27.5^{\circ},d}$ on the RIS switches. Finally, Fig. 14 compares the measured scanned angles on the same plot. The measurements confirm the capability of the RIS to scan in the $\pm 60^{\circ}$ range maintaining a single main lobe. We note here, that the beam scanning resolution is limited by the 1-bit phase quantization. As such, the beam step (angular distance between successive main lobes) is approximately equal to the beam's half-power beamwidth (HPBW). In this work, the HPBW is approximately 6 degrees resulting in a beam step of 6 degrees when beam steering is close to the boresight. The step increases when the scanning to wider angles according to the HPBW. Additionally, the side lobe level (SLL) is maintained below -7 dB for more than 100 MHz bandwidth (5.75-5.85 GHz) and below

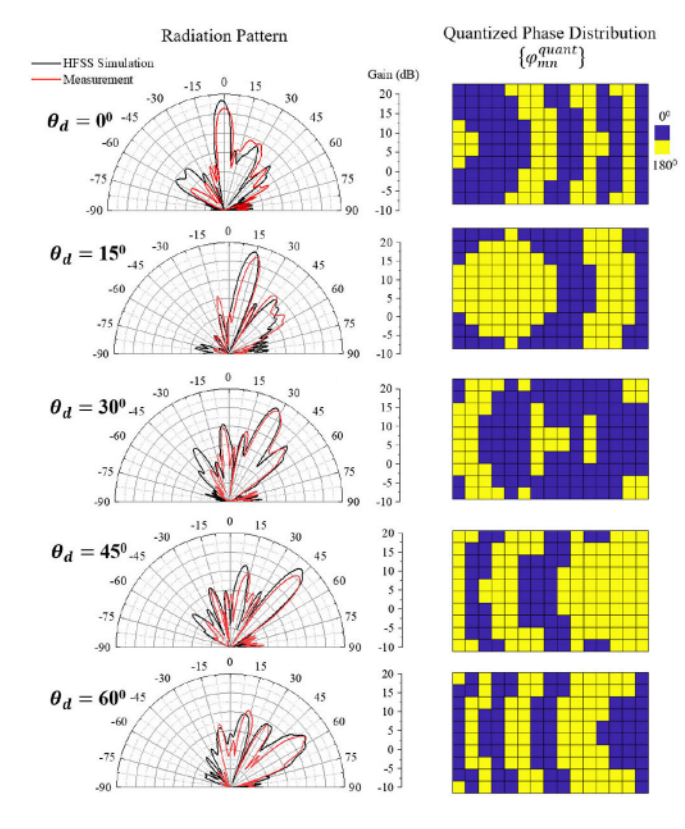


FIGURE 13. Characterization of the RIS beamforming for various reflection angles θ_d at 5.8 GHz. Left column: Comparison between computed and measured radiation patterns. Right column: Quantized (1-bit) phase shift distribution Φ^{quant} on the RIS surface to generate the respective radiation patterns.

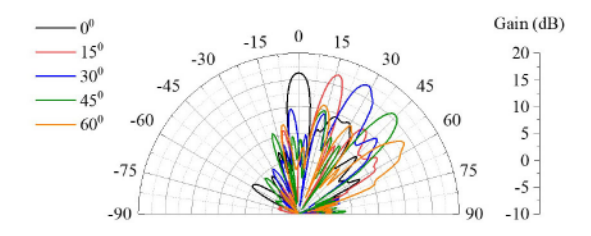


FIGURE 14. Comparison of RIS measured radiation patterns for five θ_d angles.

-5 dB for more than 400 MHz at $\theta_d = 30^\circ$. Finally, the maximum gain has a variation of less than 2.5 dB between 5.7-5.9 GHz for all measured incident angles.

IV. INTEGRATING THE RIS INTO A WIRELESS COMMUNICATION TESTBED

To demonstrate the potential of reconfigurable intelligent surfaces, we integrate the fabricated prototype, described in Section III, into a wireless communication testbed. In this section, we describe the developed testbed and beam selection process.

A. TESTBED DESCRIPTION

As illustrated in Fig. 15, our RIS-integrated wireless communication testbed consists of (i) a single-antenna transmitter, (ii) a single-antenna receiver, and (iii) the RIS. Next, we summarize the key aspects of the testbed.



FIGURE 15. The RIS-assisted wireless communication system consists of an RIS, a transmitter (BS), and a receiver (UE). The transmitter and receiver are portable and can be placed in the far-field of the RIS surface.

- *Transmitter:* We consider a single-antenna transmitter that is implemented using an NI USRPs 2901 operating at 5.8 GHz. The USRP is connected to a horn antenna with a 18.5 dBi gain, emulating the antenna gain of a BS. As will be explained shortly, the transmitter operation is controlled by a Raspberry Pi that is wirelessly controlled (over a 2.4 GHz channel).
- Receiver: Similar to the transmitter, the communication receiver is implemented using an NI USRP 2901 operating at the 5.8 GHz band. The USRP is connected to either a dipole antenna or a horn antenna with 12.5 dBi gain. The receiver is controlled by a laptop that manages the overall operation of the RIS-integrated wireless communication system.
- RIS: The developed RIS, consisting of 160 elements (16 × 10) is placed and leveraged in reflecting the transmitted signal to the receiver direction. Section III provides a detailed description for the design and fabrication of the adopted RIS.

The developed RIS-integrated wireless communication system operates at the sub-6GHz band with a center frequency of 5.8 GHz and a 20 MHz bandwidth. The system adopts an OFDM transmission/reception with 64 subcarriers. In the next subsection, we describe the operation framework including the selection of the reflection beamforming codewords at the RIS surface.

B. TESTBED OPERATION AND BEAM SELECTION

The main objective of the developed testbed is to evaluate the coverage gains when using an RIS. Toward this objective, we adopt the following operation framework. For given locations of the transmitter and receiver, the central controller triggers the transmitter to send OFDM-based pilot sequences. During this transmission, the controller wirelessly orders the Raspberry Pi that is controlling the RIS configurations to switch between the N_iN_d beams in the codebook \mathcal{P} . With this beam training, the receiver measures the power of the received signal r_k , from equation (4), and selects the optimal RIS configuration ψ^* that solves

$$\overline{\psi}^{\star} = \arg \max_{\overline{\psi} \in \mathcal{P}} \sum_{k=1}^{K} \left| r_k \left(\overline{\psi} \right) \right|^2, \tag{19}$$

where $r_k(\overline{\psi})$ is the received signal at the k-th subcarrier when the reflection beam codeword $\overline{\psi}$ is used by the RIS.

FIGURE 16. Measurement Setup 1 (ASU Campus Parking Lot). To test the RIS' electronic beamscanning capabilities in the field, the RIS is illuminated from the boresight direction ($\hat{\sigma}_I = 0$) and the reflected signal is recorded at various angles and distances. [Inset: RIS mounted on a the tripod.]

For the 1-bit codebook, \mathcal{P} , we follow the approach described in Section II-B to design it. The exact angular range and number of beams for the codebook adopted in the field measurements are provided in Section V.

V. FIELD TESTS AND RESULTS

In this section, we present the results of our field tests that evaluate the beamforming capabilities and coverage improvement of the developed RIS-based wireless communication system. First, we describe the setups adopted in the measurement campaigns in Section V-A before demonstrating the results in the following subsections. It is worth mentioning that all our measurement campaigns are conducted outdoors to account for wave propagation phenomena that occur in real-world scenarios, including scattering from the terrain, posts, and edge diffraction. Therefore, the results of these campaigns draw important insights into the actual performance of RISs in realistic wireless communication deployments.

A. MEASUREMENT SETUPS

In this subsection, we describe the two adopted setups, namely the ASU parking lot and the ASU Gammage Memorial Auditorium, where our measurements are performed.

Measurement Setup 1 (ASU Campus Parking Lot): To characterize the beamforming codebook in an LoS real-world scenario, we carried out the measurements in a parking lot. The satellite image of the parking lot with the measurement setup overlaid is shown in Fig. 16. The setup consists of the prototype-RIS mounted on a tripod, a C-band corrugated conical horn antenna with a gain of 12.5 dBi used as the feed, and a C-band pyramidal horn with a gain of 18.5 dBi used on the receiver. The feed and the receiver horns were respectively connected to transmitting and receiving USRP modules. The feed horn is positioned in front of the RIS at 5 m distance from the surface. The tripod-mounted-RIS is depicted in the inset of Fig. 16. The receiver is positioned at a distance of 10 m in front of the the RIS and rotated in a circular arc from 0°-60° to capture the deflected signals from the RIS. Further, to characterize the pathloss, the measurements were repeated at 20 m and 40 m from the RIS.

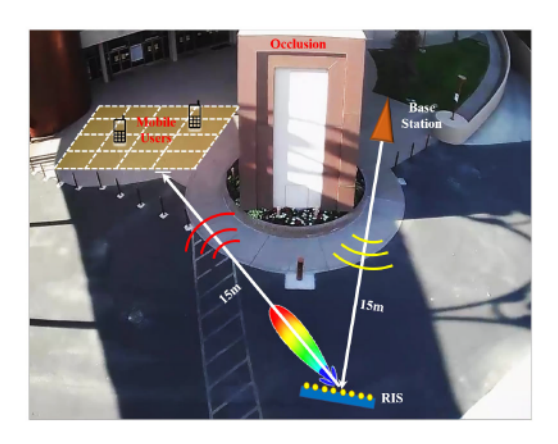


FIGURE 17. Measurement Setup 2 (ASU Gammage Memorial Auditorium). In this field test, a strong occlusion (blockage) exists between the BS and the mobile user. The RIS is strategically placed to leverage its beamscanning capabilities in extending the coverage to the LoS-obstructed mobile users.

Measurement Setup 2 (ASU Gammage Memorial Auditorium): To emulate a user environment with significant signal degradation, we carried out the coverage measurements around the entrance of ASU's Gammage Memorial Auditorium, shown in Fig. 17. Here, the base station is modeled using a 19 dBi horn antenna placed on one side of a tall (5 m) and thick (2 m) concrete wall, covering the north and eastern side of the outdoor area of the venue. On the other side of the wall, the receiver uses an ommi-directional antenna and moves in the area in front of the venue entrance. The concrete wall serves as an occlusion between the transmitter and the receiver, thus we examine the level of the received signal with and without the use of the RIS.

B. CHARACTERIZATION OF THE BEAMFORMING CODEBOOK

Here, we present the results obtained from the field measurements carried out to characterize the beam-scanning capabilities of the proposed RIS. A 20 MHz bandwidth OFDM signal centered around 5.8 GHz is coupled to the feed horn from the transmitting USRP module. The feed horn is aligned in front of the RIS such that it illuminates the RIS from broadside. The reflected signals are recorded using a receiver horn antenna along a 10°-60° arc with a radius of 10 m at every 2.5°. After beam-scanning at every point, we form a reception pattern for every RIS scanning angle. The 3D surface plot of Fig. 18 shows the beamforming capability of the RIS proposed in this work. As the beams from the RIS are scanned from 0°-60° employing the beamforming codebook, the peak power is received at the corresponding receiver location. A 5° offset between the receiver positions and RIS beam directions, noticed in the figure, is attributed to localization errors in the measurements setup due to the large distances between the RIS, transmitter, and receiver.

The received power at an exemplary angle of 40° from the broadside is shown in the inset of Fig. 18. For receiver angles less than 20°, coupling is noticed between the transmitter and the receiver. This is primarily due to the transmitter's

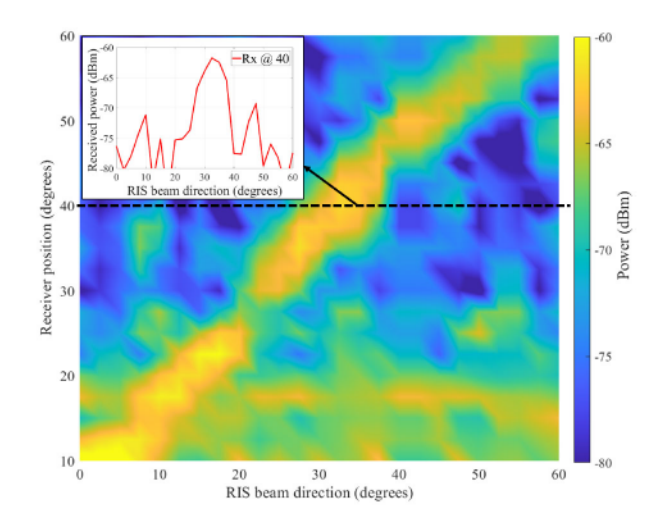


FIGURE 18. Evaluating the RIS' electronic beamscanning (azimuth plane). The high receive power at the diagonal line confirms the agreement between the codebook beam directions and the receiver location (which is moving along a circular path, as shown in Fig. 16). [Inset: 2D plot of the received signal when the receiver is oriented 40° from the broadsidel.

backlobes as well as its close proximity to the receiver for directions near broadside. This is an artifact due to the limitations of the measurement setup and would not be present in a deployment where the transmitter is much farther or blocked by an occlusion. Nevertheless, the power corresponding to the the desired direction is still sufficiently high to offset this coupling effect and the receiver is able to detect the RIS beam. Using as a reference the SNR of the signal when the receiver is not aligned with the RIS beam, Fig. 18 shows that we can achieve around 18-20 dB SNR gain in the considered deployment scenario. It is worth mentioning here that these beamforming gains can potentially be improved if these codebooks are further optimized to match the RIS hardware impairments and the surrounding environment [51], [52]. It is also important to note here that due to the 1-bit phase quantization, there is a symmetric beam that appears around the specular direction. In Fig. 17, however, we are only illustrating the RIS beam that is the desired direction (towards the blocked users).

C. PATHLOSS MEASUREMENTS

To characterize the pathloss, similar beamforming measurements were repeated at distances of 20 m and 40 m from the RIS. Fig. 19 depicts the change in the received power levels, at few nominal angles (10°, 20° and 30°) from broadside, as a function of distance from the RIS. As expected, the pathloss increases as the distance from the RIS increases as well as when the beam deviates away from the broadside direction.

D. SIGNAL COVERAGE MEASUREMENTS

In this section, we present the results of the signal coverage measurements. The goal is to evaluate the improvement of the received signal power for a mobile user that employs an omnidirectional antenna. This experiment was done using the measurement setup 2 (ASU Gammage Memorial

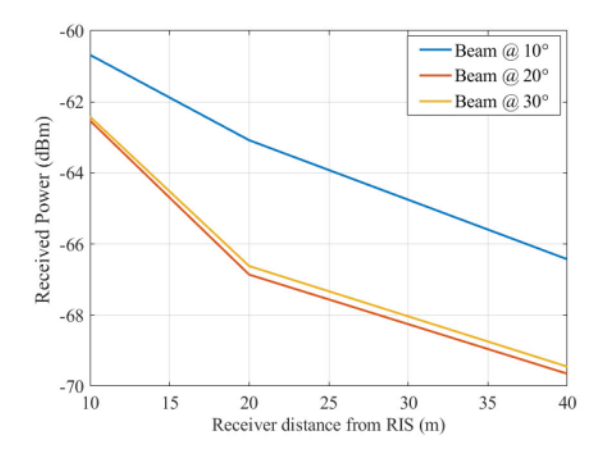
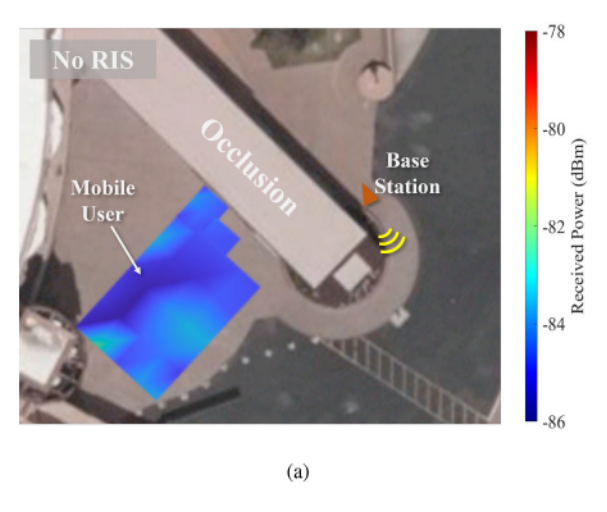


FIGURE 19. Path loss as a function of distance: The receiver is fixed at various directions ($\theta_d = 10^\circ, 20^\circ, 30^\circ$) from broadside and the distance between the RIS and the receiver is increased from 10 m to 40 m.



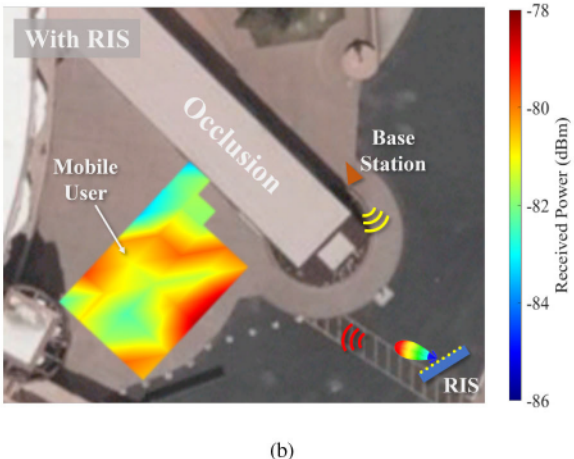


FIGURE 20. Field test with strong occlusion between the base station and the mobile user. (a) Coverage map without the RIS and (b) Coverage map using the RIS. The field measurements indicate an average SNR gain of \sim 6 dB (max 8 dB) when the RIS is deployed.

Auditorium), described in Section V-A. In the absence of RIS, the received signal on a 28-point grid is low due to the occlusion (signal blockage) from the large wall, as shown in the coverage map in Fig. 20(a). To evaluate the potential

of the RIS in expanding the signal coverage, we place the RIS at a strategic place such that the RIS is in LoS of both the base station and the occluded area (in front of the venue entrance). As such, the RIS intercepts the signal from the base station and redirects it to the mobile user. In this scenario, the path from the base station to the RIS to the UE ranges between 30-40 meters depending on the grid position. As the user moves to each grid position, the RIS scans the codebook beams horizontally to find the optimum signal reception. The second coverage map in Fig. 20(b) shows the improved received signal level using the RIS beam scanning. The SNR improvement along the occluded/blocked region is up to 8 dB with an average of 6 dB. We note here that the SNR improvement is a function of the RIS size, thus a reasonably 10 times larger aperture (1,600 elements) would result in 28 dB SNR improvement for the same coverage scenario. The 20 dB improvement is due the fact that the received signal depends on the square of the RIS area, as derived from equations (1) and (3).

VI. CONCLUSION

In this work, we developed a proof-of-concept prototype for reconfigurable intelligent surfaces and evaluated their potential gains in real-world environments and practical settings. In particular, we designed and fabricated a sub-6 GHz 160element RIS prototype, which relies on a planar single layer reconfigurable reflectarray (no vias) capable of scanning in both azimuth and elevation planes. Thanks to the simplicity of the geometry and the capability to operate with single-bit switches, the proposed design can be directly scaled to higher frequencies such as mmWave and THz systems using either RF PIN switches, transistor based switches (e.g., CMOSbased), or tunable materials (e.g., graphene). For this RIS prototype, we characterized the beamforming capabilities for both the passive (no RF diodes) and active implementations which achieved a half-power-beamwidth (HPBW) of approximately 9 degrees and 16 degrees on the azimuth and elevation planes, respectively. Then, we integrated the RIS into a wireless communication system to accurately evaluate its beamforming and coverage gains in realistic communication scenarios. Our results indicated that the developed RIS system can provide around 20 dB SNR gain when both the transmitter/receiver use directional antennas and when they are at distances of 5 m and 10 m from the RIS. Further, when the average BS \rightarrow RIS \rightarrow UE distance is 35 m, with blocked LoS link, and when only one side uses a directional antenna while the other side adopts an omni-directional antenna, an SNR gain of 8 dB is achievable. This gain can be further increased by increasing the size of the RIS. For example, a ten-fold increase in the area of the RIS to a moderate 1,600-element array will further increase the SNR by 20.

This work has shown that RISs is a promising technology in extending wireless coverage in scenarios where occlusions are strong, even if the RIS is in the far field of both base station and mobile user. Additionally, RISs have the potential to operate in extremely low power levels which is important for i) sustainable wireless communications and ii) to enable deployments where access to power supply is limited or even non-existent. The current non-optimized prototype consumes less than 0.4 Watt (including the biasing circuitry). As an alternative to PIN diodes, transistor-based switches [50] are promising devices for extremely low power consumption RISs. The low leakage current of field-effect-transistor (FET) switches may consume less than 4 μ Watt of DC power for an RIS with 10,000 switches. Finally, beamforming performance can be improved in future designs by eliminating the grating lobes that appear in the opposite direction to the main beam. This improvement can be achieved by adding a fixed, random phase delay on each unit cells and mitigate the quantization errors stemming from low-bit sampling [38], [47].

ACKNOWLEDGMENT

We would like to thank Rogers Inc. Chandler, AZ for providing the substrates for the implementation of all prototypes presented in this work. Many thanks to Craig Birtcher for his help in the radiation pattern measurements in the Compact Antenna Test Range.

REFERENCES

- C. Liaskos, S. Nie, A. Tsioliaridou, A. Pitsillides, S. Ioannidis, and I. Akyildiz, "A new wireless communication paradigm through software-controlled metasurfaces," *IEEE Commun. Mag.*, vol. 56, no. 9, pp. 162–169, Sep. 2018.
- [2] E. Basar, M. Di Renzo, J. De Rosny, M. Debbah, M.-S. Alouini, and R. Zhang, "Wireless communications through reconfigurable intelligent surfaces," *IEEE Access*, vol. 7, pp. 116753–116773, 2019.
- [3] M. Di Renzo et al., "Smart radio environments empowered by reconfigurable intelligent surfaces: How it works, state of research, and the road ahead," *IEEE J. Sel. Areas Commun.*, vol. 38, no. 11, pp. 2450–2525, Nov. 2020.
- [4] A. Taha, M. Alrabeiah, and A. Alkhateeb, "Enabling large intelligent surfaces with compressive sensing and deep learning," *IEEE Access*, vol. 9, pp. 44304–44321, 2021.
- [5] X. Ying, U. Demirhan, and A. Alkhateeb, "Relay aided intelligent reconfigurable surfaces: Achieving the potential without so many antennas," 2020, arXiv:2006.06644.
- [6] M. Nemati, J. Park, and J. Choi, "RIS-assisted coverage enhancement in millimeter-wave cellular networks," *IEEE Access*, vol. 8, pp. 188171–188185, 2020.
- [7] E. Moro, I. Filippini, A. Capone, and D. De Donno, "Planning mmwave access networks with reconfigurable intelligent surfaces," 2020, arXiv:2105.11755.
- [8] M. He, W. Xu, and C. Zhao, "RIS-assisted broad coverage for mmWave massive MIMO system," in *Proc. IEEE Int. Conf. Commun.* Workshops (ICC Workshops), Montreal, QC, Canada, 2021, pp. 1–6.
- [9] M. Nemati, B. Maham, S. R. Pokhrel, and J. Choi, "Modeling RIS empowered outdoor-to-indoor communication in mmWave cellular networks," *IEEE Trans. Commun.*, vol. 69, no. 11, pp. 7837–7850, Nov. 2021.
- [10] X. Mu, Y. Liu, L. Guo, J. Lin, and R. Schober, "Simultaneously transmitting and reflecting (STAR) RIS aided wireless communications," *IEEE Trans. Wireless Commun.*, early access, Oct. 13, 2021, doi: 10.1109/TWC.2021.3118225.
- [11] J. Xu, Y. Liu, X. Mu, and O. A. Dobre, "STAR-RISs: Simultaneous transmitting and reflecting reconfigurable intelligent surfaces," *IEEE Commun. Lett.*, vol. 25, no. 9, pp. 3134–3138, Sep. 2021.
- [12] J. Choi, G. Kwon, and H. Park, "Multiple intelligent reflecting surfaces for capacity maximization in LOS MIMO systems," *IEEE Wireless Commun. Lett.*, vol. 10, no. 8, pp. 1727–1731, Aug. 2021.

- [13] O. Özdogan, E. Björnson, and E. G. Larsson, "Using intelligent reflecting surfaces for rank improvement in MIMO communications," in *Proc. IEEE Int. Conf. Acoust. Speech Signal Process. (ICASSP)*, Barcelona, Spain, 2020, pp. 9160–9164.
- [14] H. Zhang, H. Zhang, B. Di, K. Bian, Z. Han, and L. Song, "Metalocalization: Reconfigurable intelligent surface aided multi-user wireless indoor localization," *IEEE Trans. Wireless Commun.*, vol. 20, no. 12, pp. 7743–7757, Dec. 2021.
- [15] E. Čišija, A. M. Ahmed, A. Sezgin, and H. Wymeersch, "RIS-aided mmWave MIMO radar system for adaptive multi-target localization," in *Proc. IEEE Stat. Signal Process. Workshop (SSP)*, Rio de Janeiro, Brazil, 2021, pp. 196–200.
- [16] L. Yang, J. Yang, W. Xie, M. O. Hasna, T. Tsiftsis, and M. D. Renzo, "Secrecy performance analysis of RIS-aided wireless communication systems," *IEEE Trans. Veh. Technol.*, vol. 69, no. 10, pp. 12296–12300, Oct. 2020.
- [17] Y. Ai, F. A. P. deFigueiredo, L. Kong, M. Cheffena, S. Chatzinotas, and B. Ottersten, "Secure vehicular communications through reconfigurable intelligent surfaces," *IEEE Trans. Veh. Technol.*, vol. 70, no. 7, pp. 7272–7276, Jul. 2021.
- [18] A. U. Makarfi, K. M. Rabie, O. Kaiwartya, X. Li, and R. Kharel, "Physical layer security in vehicular networks with reconfigurable intelligent surfaces," in *Proc. IEEE 91st Veh. Technol. Conf. (VTC-Spring)*, Antwerp, Belgium, May 2020, pp. 1–6.
- [19] M. Wijewardena, T. Samarasinghe, K. T. Hemachandra, S. Atapattu, and J. S. Evans, "Physical layer security for intelligent reflecting surface assisted two-way communications," *IEEE Commun. Lett.*, vol. 25, no. 7, pp. 2156–2160, Jul. 2021.
- [20] M. H. Khoshafa, T. M. N. Ngatched, and M. H. Ahmed, "Reconfigurable intelligent surfaces-aided physical layer security enhancement in D2D underlay communications," *IEEE Commun. Lett.*, vol. 25, no. 5, pp. 1443–1447, May 2021.
- [21] N. Yu et al., "Light propagation with phase discontinuities: Generalized laws of reflection and refraction," Science, vol. 334, no. 6054, pp. 333–337, Oct. 2011. [Online]. Available: https://science.sciencemag.org/content/334/6054/333
- [22] S. V. Hum and J. Perruisseau-Carrier, "Reconfigurable reflectarrays and array lenses for dynamic antenna beam control: A review," *IEEE Trans. Antennas Propag.*, vol. 62, no. 1, pp. 183–198, Jan. 2014.
- [23] J. Ma, R. Shrestha, W. Zhang, L. Moeller, and D. M. Mittleman, "Terahertz wireless links using diffuse scattering from rough surfaces," *IEEE Trans. THz Sci. Technol.*, vol. 9, no. 5, pp. 463–470, Sep. 2019. [Online]. Available: https://ieeexplore.ieee.org/document/8788543/
- [24] I. Rodriguez et al., "Analysis of 38 GHz mmWave propagation characteristics of urban scenarios," in Proc. 21st Eur. Wireless Conf., Budapest, Hungary, May 2015, pp. 1–8.
- [25] C. Huang, A. Zappone, G. C. Alexandropoulos, M. Debbah, and C. Yuen, "Reconfigurable intelligent surfaces for energy efficiency in wireless communication," *IEEE Trans. Wireless Commun.*, vol. 18, no. 8, pp. 4157–4170, Aug. 2019.
- [26] G. Zhou, C. Pan, H. Ren, K. Wang, and K. K. Chai, "RIS-aided mmWave transmission: A stochastic majorization-minimization approach," in *Proc. IEEE Int. Conf. Commun.*, Montreal, QC, Canada, 2021, pp. 1–6.
- [27] J. Ye, S. Guo, and M.-S. Alouini, "Joint reflecting and precoding designs for SER minimization in reconfigurable intelligent surfaces assisted MIMO systems," *IEEE Trans. Wireless Commun.*, vol. 19, no. 8, pp. 5561–5574, Aug. 2020.
- [28] Q. Zhu, H. Li, R. Liu, M. Li, and Q. Liu, "Hybrid beamforming and passive reflection design for RIS-assisted mmWave MIMO systems," in *Proc. IEEE Int. Conf. Commun. Workshops (ICC Workshops)*, Montreal, QC, Canada, 2021, pp. 1-6.
- [29] M. Yue, L. Liu, and X. Yuan, "Practical RIS-aided coded systems: Joint precoding and passive beamforming," *IEEE Wireless Commun. Lett.*, vol. 10, no. 11, pp. 2345–2349, Nov. 2021.
- [30] H. Yang et al., "A programmable metasurface with dynamic polarization, scattering and focusing control," Sci. Rep., vol. 6, pp. 1–11, Oct. 2016.
- [31] T. J. Cui, M. Q. Qi, X. Wan, J. Zhao, and Q. Cheng, "Coding metamaterials, digital metamaterials and programmable metamaterials," *Light Sci. Appl.*, vol. 3, no. 10, p. e218, 2014. [Online]. Available: www.nature.com/lsa

- [32] X. Wan, M. Q. Qi, T. Y. Chen, and T. J. Cui, "Field-programmable beam reconfiguring based on digitally-controlled coding metasurface," Sci. Rep., vol. 6, pp. 1–8, Feb. 2016. [Online]. Available: http://dx.doi.org/10.1038/srep20663
- [33] V. Arun and H. Balakrishnan, "RFocus: Beamforming using thousands of passive antennas," in *Proc. 17th USENIX Symp. Netw. Syst. Des. Implement. (NSDI)*, Feb. 2020, pp. 1047–1061.
- [34] X. Pei et al., "RIS-aided wireless communications: Prototyping, adaptive beamforming, and indoor/outdoor field trials," Feb. 2021, arXiv:2103.00534.
- [35] H. Kamoda, T. Iwasaki, J. Tsumochi, T. Kuki, and O. Hashimoto, "60-GHz electronically reconfigurable large reflectarray using singlebit phase shifters," *IEEE Trans. Antennas Propag.*, vol. 59, no. 7, pp. 2524–2531, Jul. 2011.
- [36] D. Headland et al., "Terahertz reflectarrays and nonuniform metasurfaces," IEEE J. Sel. Topics Quantum Electron., vol. 23, no. 4, Jul./Aug. 2017, Art. no. 8500918.
- [37] W. A. Vitale et al., "Modulated scattering technique in the terahertz domain enabled by current actuated vanadium dioxide switches," Sci. Rep., vol. 7, no. 1, Feb. 2017, Art. no. 41546. [Online]. Available: http://www.nature.com/articles/srep41546
- [38] B. G. Kashyap, P. C. Theofanopoulos, Y. Cui, and G. C. Trichopoulos, "Mitigating quantization lobes in mmWave low-bit reconfigurable reflective surfaces," *IEEE Open J. Antennas Propag.*, vol. 1, pp. 604–614, 2020.
- [39] P. C. Theofanopoulos and G. C. Trichopoulos, "A novel 2-bit graphene reconfigurable reflectarray," in *Proc. IEEE Int. Symp. Antennas Propag. North Amer. Radio Sci. Meeting*, Montreal, QC, Canada, Jul. 2020, pp. 1701–1702.
- [40] P. C. Theofanopoulos and G. C. Trichopoulos, "Modeling and analysis of terahertz graphene switches for on-wafer coplanar transmission lines," *J. Infrared Millimeter THz Waves*, vol. 41, no. 7, pp. 758–775, Jul. 2020. [Online]. Available: http://link.springer.com/ 10.1007/s10762-020-00711-4
- [41] P. C. Theofanopoulos, S. Ageno, Y. Guo, S. Kale, Q. H. Wang, and G. C. Trichopoulos, "High-yield fabrication method for high-frequency graphene devices using titanium sacrificial layers," *J. Vac. Sci. Technol. B*, vol. 37, no. 4, Jul. 2019, Art. no. 41801. [Online]. Available: http://avs.scitation.org/doi/10.1116/1.5098324
- [42] J. Huang and J. Encinar, Reflectarray Antennas. Piscataway, NJ, USA: IEEE Press, 2008.
- [43] H. Yang et al., "A study of phase quantization effects for reconfigurable reflectarray antennas," *IEEE Antennas Wireless Propag. Lett.*, vol. 16, pp. 302–305, 2017.
- [44] D. M. Pozar, S. D. Targonski, and H. D. Syrigos, "Design of millimeter wave microstrip reflectarrays," *IEEE Trans. Antennas Propag.*, vol. 45, no. 2, pp. 287–296, Feb. 1997.
- [45] S. V. Hum, M. Okoniewski, and R. J. Davies, "Modeling and design of electronically tunable reflectarrays," *IEEE Trans. Antennas Propag.*, vol. 55, no. 8, pp. 2200–2210, Aug. 2007.
- [46] F. Venneri, S. Costanzo, and G. Di Massa, "Design and validation of a reconfigurable single varactor-tuned reflectarray," *IEEE Trans. Antennas Propag.*, vol. 61, no. 2, pp. 635–645, Feb. 2013.
- [47] J. Yin, Q. Wu, Q. Lou, H. Wang, Z. N. Chen, and W. Hong, "Single-beam 1 bit reflective metasurface using prephased unit cells for normally incident plane waves," *IEEE Trans. Antennas Propag.*, vol. 68, no. 7, pp. 5496–5504, Jul. 2020.
- [48] Q. Wu and R. Zhang, "Beamforming optimization for wireless network aided by intelligent reflecting surface with discrete phase shifts," *IEEE Trans. Commun.*, vol. 68, no. 3, pp. 1838–1851, Mar. 2020.
- [49] B. A. Munk, Frequency Selective Surfaces: Theory and Design. Hoboken, NJ, USA: Wiley, 2005.
- [50] S. Venkatesh, X. Lu, H. Saeidi, and K. Sengupta, "A high-speed programmable and scalable terahertz holographic metasurface based on tiled CMOS chips," *Nat. Electron.*, vol. 3, no. 12, pp. 785–793, Dec. 2020. [Online]. Available: http://www.nature.com/articles/s41928-020-00497-2
- [51] Y. Zhang, M. Alrabeiah, and A. Alkhateeb, "Reinforcement learning of beam codebooks in millimeter wave and terahertz MIMO systems," 2021, arXiv:2102.11392.
- [52] M. Alrabeiah, Y. Zhang, and A. Alkhateeb, "Neural networks based beam codebooks: Learning mmWave massive MIMO beams that adapt to deployment and hardware," 2020, arXiv:2006.14501.